Coupling turbulent flow with blade aeroelastics and control modules in large-eddy simulation of utility-scale wind turbines ⊞ ✓

Christian Santoni ⓘ ; Ali Khosronejad ✉ ⓘ ; Xiaolei Yang (杨晓雷) ⓘ ; Peter Seiler ⓘ ; Fotis Sotiropoulos ⓘ

Check for updates

View Online

Export Citation

08 April 2024 03:48:04

Coupling turbulent flow with blade aeroelastics and control modules in large-eddy simulation of utility-scale wind turbines [EP]

Christian Santoni,[1] [iD] Ali Khosronejad,[1,a)] [iD] Xiaolei Yang (杨晓雷),[2] [iD] Peter Seiler,[3] [iD] and Fotis Sotiropoulos[4] [iD]

AFFILIATIONS

[1]Department of Civil Engineering, Stony Brook University, Stony Brook, New York 11794, USA
[2]LNM, Institute of Mechanics, Chinese Academy of Sciences, Beijing 100190, China
[3]Electrical Engineering and Computer Science, University of Michigan, Ann Arbor, Michigan 48109, USA
[4]Mechanical & Nuclear Engineering, Virginia Commonwealth University, Richmond, Virginia 23284, USA

[a)]Author to whom correspondence should be addressed: ali.khosronejad@stonybrook.edu

ABSTRACT

We present a large-eddy simulation framework capable of control co-design of large wind turbines, coupling the turbulent flow environment with blade aeroelastics and turbine controllers. The geometry and aerodynamics of the rotor blades and the turbine nacelle are parameterized using an actuator surface model. The baseline collective pitch control and individual pitch control (IPC) algorithms, consisting of a single-input, single-output proportional–integral controller and two integral controllers, respectively, are incorporated into the simulation framework. Furthermore, a second-order model based on the Euler–Bernoulli beam theory is implemented to describe the blade deformation. Simulations are carried out to investigate the impact of collective and individual pitch control strategies on the deflection of turbine blades. Our results show that the IPC reduces the blade tip deflection fluctuations in the out-of-plane direction, while the fluctuations of the blade tip deflection along the in-plane direction are barely affected by the IPC. Furthermore, the blade out-of-plane deformation fluctuation is underestimated by the one-way coupling approach compared to the two-way coupling approach. The findings of this study reveal the importance of advanced control systems in reducing the dynamic loads on wind turbine blades and underscore the potential of control co-design to reduce the levelized cost of wind energy.

Published under an exclusive license by AIP Publishing. https://doi.org/10.1063/5.0135518

I. INTRODUCTION

With an annual increase rate of 30%, wind energy is the second largest source of renewable energy in the world and one of the fastest-growing sources of electricity in the United States.[1] Researchers have been focused on reducing the levelized cost of energy (LCOE) to produce clean, renewable power at cost competitive to non-renewables. One proposed approach, among others, for decreasing the LCOE is to increase the size of wind turbines. For example, Mendoza *et al.*[2] proposed the design of a 250 m blade for a rotor capable of producing 50 MW. However, they recognize that it is necessary to reduce the mass of the blade to improve its feasibility. Recent advances in advanced materials along with control methods to reduce fatigue loads could lead to the design of lighter and more flexible blades.[1] Fatigue loads are of special consideration for larger-scale wind turbines as, because of their size, they are subjected to unbalanced large-scale loads due to the considerable variation of wind-shear-induced aerodynamic forces across the rotor diameter.

A review of wind turbine controllers by Bossanyi[3] proposed the use of feedback control to reduce the magnitude of 1P load fluctuations (where P is the blade rotational frequency) on the tower and blade. Such load fluctuations are caused by the wind shear and tower shadowing by individually pitching the turbine blades.[3] Multiple individual pitch control (IPC) strategies have been developed using multi-blade coordinate transformation to enable the use of classical control systems. For example, Bossanyi[4] applied a linear-quadratic-Gaussian (LQG) and a proportional–integral (PI) controller to reduce the load fluctuations. Also, Geyler and Caselitz,[5] Vali *et al.*,[6] and Ossmann *et al.*[7] applied the H_∞-norm optimal controller to reduce fatigue loads of the blades, and other non-rotating components such as the tower, using IPC. Most of the proposed controllers were studied using models

such as the Fatigue, Aerodynamics, Structures, and Turbulence (FAST) multiphysics tool,[8] HAWC2,[9,10] and Bladed, which consider the aeroelastic behavior of the turbine, including tower and blades. However, in these models, the aerodynamic behavior of the blades is modeled using simplified low-fidelity techniques, such as the blade element momentum (BEM) theory. To account for the unsteady aerodynamics of the wind turbine, Santoni et al.[11] coupled the actuator surface model of Yang and Sotiropoulos[23] with the IPC to perform large-eddy simulations (LES) of a turbine in a neutral atmospheric boundary layer flow using the Virtual Flow Simulator code (VFS-Wind).[18] They showed that the IPC decreased the fatigue damage to the blades caused by the wind shear, but its effect on the wake of the turbine was minimal compared to the baseline control. Nevertheless, their simulations neglected the aeroelasticity of the blades, which may impact the accuracy of the prediction of fatigue load reduction by the IPC.

To describe the unsteady aerodynamics of the wind turbine with higher fidelity (i.e., taking into account the instantaneous turbulent atmospheric flow environment), researchers have combined structural solvers with computational fluid dynamics models of varying fidelity. For example, Churchfield et al.[12] coupled the OpenFOAM and FAST models to perform LES of the turbine aerodynamics and system dynamics under stable and unstable atmospheric conditions. They demonstrated that the flapwise deformations of the blades are highly influenced by the atmospheric turbulence. Meng et al.[13] coupled the actuator line model with a rotating isotropic cantilever beam model and performed Reynolds averaged Navier–Stokes (RANS) simulations to validate their model against the FAST model. Similarly, Yu et al.[14] combined the actuator line model with a rotating beam model to conduct LES of the NREL 5 MW turbine. More recently, della Posta et al.[15] presented a modal beam-like structural solver and coupled it with an actuator line model to perform LES of the NREL 5 MW turbine. They showed that the two-way coupling method dampens the natural frequency vibrations of the turbine blades compared to the one-way coupling approach. Furthermore, della Posta et al.[16] reported that the stability of the blade deflections is highly influenced by the tower shadowing effect, creating sudden changes along the edgewise direction.

In spite of the significant advances reported in these previous studies, however, to the best of our knowledge, the effect of advanced control systems on the aeroelastic behavior of wind turbine blades has yet to be addressed. Therefore, the main contribution of this work is twofold: (1) to develop a computational tool coupling turbulent flow with blade aeroelastics and turbine control strategies; and (2) apply this tool to study the aeroelastic performance of the turbine blade with IPC and systematically investigate the ability of IPC to reduce fatigue loads. To do so, we coupled the aeroelastic model of Kallesøe[17] with the VFS-Wind code[18] to develop a fluid–structure interaction (FSI) algorithm for turbine blades. The aeroelastic model of Kallesøe[17] expands on a model proposed by Hodges and Dowell[19] for rotor blades of helicopters to take into account the pitch action, rotor speed variations, and gravity using a second-order Euler–Bernoulli beam theory describing the blade deformation/deflection. The nonlinear partial integral-differential equations of the aeroelastic model were coupled with the actuator surface model for the computation of the aerodynamic forces to compute the deflection of the turbine blades.

A major algorithmic issue affecting the stability, accuracy, and efficiency of FSI algorithms is whether a loose or strong coupling strategy is employed to couple the flow and structural solvers. Heinz[20] compared the results of loose and strong coupling strategies to show that the computationally more efficient one-way loose coupling approach, in which the equations of blade deformation are solved once per time step, could suffice in FSI of wind turbine blades. However, della Posta et al.[15,16] have shown that a two-way loose coupling approach, by considering the blade deformation velocity in the computation of the aerodynamic loads, reduces the blade vibrations, thus increasing the accuracy of the model without the added computational cost of the classical two-way strong coupling algorithm. Therefore, to minimize the computational cost, both a one-way loose coupling and della Posta et al.[15] two-way loose coupling are implemented herein with Kallesøe's structural model and in conjunction with the actuator surface model implemented in VFS-Wind.[18] To validate the resulting FSI version of the VFS-Wind code, we apply it to simulate the offshore NREL 5 MW baseline wind turbine for which the structural properties of the blade are well defined. Thereafter, the validated VFS-Wind code is employed to study the aeroelastic behavior of the Clipper Liberty C96 turbine (located at the Eolos wind energy research field station of the University of Minnesota, 20 km south of Saint Paul, Minnesota) subjected to the IPC implemented via a multi-blade coordinate transformation combined with a classical integral loop.[7]

This paper is organized as follows. A description of the governing equations is presented in Sec. II A. The actuator surface for modeling turbine blades and nacelle is presented in Sec. II B. A brief description of the turbine baseline collective pitch controller and individual pitch controller is given in Secs. II C and II D, respectively. In addition, an overview of the blade deformation equations and their discretization method is provided in Sec. II E. The coupling among the fluid flow, structure, actuator surface model, and turbine controller is described in Sec. II F. Validation of the coupling of the blade tip deflection of the NREL 5 MW turbine is discussed in Sec. II G. A description of the numerical simulations of the Eolos Clipper Liberty C96 wind turbine with the advanced IPC is given in Sec. III. In Sec. IV A, a comparative analysis of the blade tip deflection with the CPC and IPC is given. Furthermore, the influence of the blade deflection on the loads and the time-averaged velocity field in the wake of the Eolos turbine is provided in Sec. IV B. Comparisons between the one and two-way coupled structural models are discussed in Sec. IV C. Finally, the findings of the paper are summarized in Sec. V.

II. METHODOLOGY
A. Equations of flow motion

The Navier–Stokes equations are solved to describe the wind flow field past a wind turbine. These equations, in a generalized curvilinear coordinates system, are given by

$$\frac{\partial U^i}{\partial t} = \xi_l^i \left[-\frac{\partial U^j u_l}{\partial \xi^j} + \frac{1}{Re} \frac{\partial}{\partial \xi^j} \left(\frac{g^{jk}}{J} \frac{\partial u_l}{\partial \xi^k} \right) - \frac{\partial}{\partial \xi^j} \left(\frac{\xi_l^j p}{J} \right) - \frac{\partial \tau_{lj}}{\partial \xi^j} + f_l \right],$$

(1)

$$J \frac{\partial U^i}{\partial \xi^i} = 0,$$

(2)

where u_l is the filtered Cartesian velocity component along the l-direction, and p is the pressure. The contravariant volume flux, U^i, is given

08 April 2024 03:48:04

by $U^i = (\xi^i_m/J)u_m$, where ξ^i_m is the Jacobian of the curvilinear transformation and J its determinant. The contravariant metric tensor is given by $g^{jk} = \xi^j_l \xi^k_l$. The Reynolds number is defined as $Re = \rho U_\infty D/\mu$, where U_∞ is the wind velocity far from the bottom surface, D is the wind turbine rotor diameter, ρ is the air density, and μ is the kinematic viscosity. The sub-grid stresses τ_{lj} are modeled using the dynamic eddy viscosity model.[21] The external forces per unit volume, f_l, are computed using actuator surface models for the wind turbine blades and nacelle. In VFS-Wind, the spatial derivatives in the momentum equations are discretized in space using three-point central-differencing and advanced in time using the Crank-Nicolson scheme.[18] The resulting non-solenoidal velocity field obtained from solving the momentum equation is projected into a divergence-free velocity vector field using the fractional step method.[22]

B. Wind turbine model

The blades and nacelle of the wind turbine are modeled using the actuator surface model proposed by Yang and Sotiropoulos.[23] According to this model, the turbine blades and nacelle are discretized with an unstructured triangular mesh (Lagrangian system) immersed into the background Cartesian of curvilinear grid (Eulerian system) used to solve the flow equations (see Fig. 1). The lift f_L and drag f_D over the blade are computed using the blade element theory[24] and are given by

$$f_L = \frac{1}{2} C_L(\alpha)\rho U_{rel}^2 c, \tag{3}$$

$$f_D = \frac{1}{2} C_D(\alpha)\rho U_{rel}^2 c, \tag{4}$$

where C_L and C_D are the lift and drag coefficients of the airfoil, respectively, α is the angle of attack, ρ is the fluid density, and c is the chord length. The relative velocity, U_{rel}, is computed as

$$U_{rel} = \sqrt{U_x^2 + (U_\theta - \omega r)^2}, \tag{5}$$
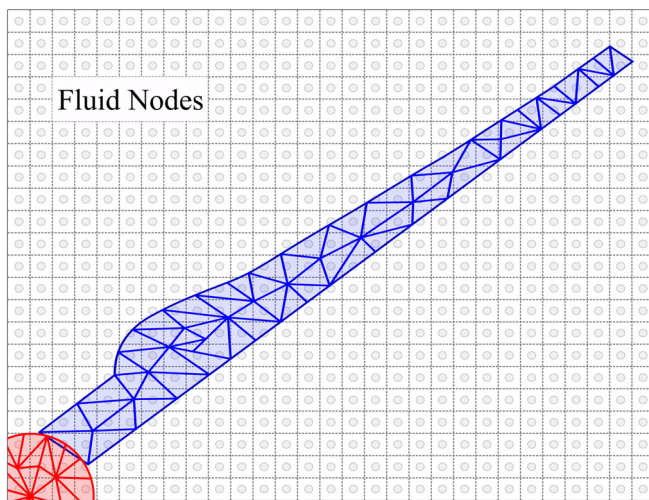

FIG. 1. Schematic of the blade (blue lines) and nacelle (red lines) actuator surface unstructured grid over the fluid Eulerian grid nodes (filled circles).

where ω is the rotor angular velocity, and r is the distance from the rotor center to the blade element. The axial velocity, U_x, and azimuthal velocity, U_θ, are computed by averaging velocity over the chord, obtained from the flow solver, and projected over the blade surface. The blade element theory assumes that the forces on a blade element can be computed from the airfoil characteristics using the angle of attack and incident resultant velocity at each element.[24] Therefore, the lift and drag coefficients are obtained from a lookup table by computing the local angle of attack of each blade section given by

$$\alpha = \left(\frac{U_x}{U_\theta - \omega r}\right) - \varphi, \tag{6}$$

where φ is the blade twist angle. Three-dimensional and rotational effects of the blades are taken into account by correcting the lift and drag coefficient using the stall delayed model of Du and Selig.[25] Moreover, losses due to the tip vortex formation are considered by applying a tip loss correction factor to the aerodynamic forces, as in Shen et $al.$[26] The force at each radial location is then computed as $f_i = (f_{L_i} + f_{D_i})/c$ and distributed uniformly along the chordwise direction on the Lagrangian grid. With reference to Fig. 1, the resulting forces are distributed from the unstructured Lagrangian blade grid into the structured Eulerian grid system, where the equations of fluid motion are solved using a discrete delta function approach (see Yang and Sotiropoulos[23] for details).

The nacelle geometry is parameterized into the flow domain as an impermeable body with a distributed friction force over its surface. The impermeability of the nacelle (no flux condition) is implemented via a direct forcing immersed boundary approach with the required normal force computed as follows:

$$f_n = \frac{\rho h \tilde{u}_n}{\Delta t}, \tag{7}$$

where $\tilde{u}_n$ is the velocity normal to the actuator surface of the nacelle, and $h = (\Delta x \Delta y \Delta z)^{1/3}$ is the Eulerian grid length scale. The tangential force per unit area is given by

$$f_\tau = \frac{1}{2} \rho C_f U^2, \tag{8}$$

where U is the incoming wind speed, and C_f is the skin friction coefficient obtained from the following empirical relation:[27]

$$C_f = 0.37(\log Re_X)^{-2.584}, \tag{9}$$

where Re_X is the Reynolds number calculated from the incoming velocity and the distance from the leading edge of the nacelle. The resulting forces are projected into the Eulerian grid using a smoothed cosine discrete delta function[28] and are incorporated into the equations of motion via the force term f [see Eq. (1)]. Details of the actuator surface model can be found in Yang and Sotiropoulos.[23]

C. Baseline control system: Collective pitch control (CPC)

The baseline controller of the wind turbine serves two purposes: (1) to maintain the turbine operation at maximum efficiency and (2) to regulate the angular velocity of the rotor to avoid structural damage. The angular velocity of the rotor delimits the turbine control operation and is indicated by the region naming convention (regions 1, 2, 2.5, and 3).

At wind speeds below rated by the manufacturer (region 2), the turbine controller maximizes the power production of the turbine by optimizing the aerodynamic efficiency of the rotor. This is done by regulating the angular velocity of the rotor by setting the generator torque at

$$\tau_g = \frac{\pi \rho R^5 C_{p,\max}}{2\lambda_{opt}^3 G^3}\omega_g^2, \tag{10}$$

where $C_{p,\max}$ is the maximum power coefficient at the optimal tip-speed ratio of λ_{opt}, R is the rotor radius, G is the gearbox ratio, and ω_g is the generator angular velocity.[29] For wind speeds higher than rated (region 2.5–3), the controller objective is to maintain the angular velocity at its rated value. This is performed to avoid any structural damage that the aerodynamic and inertial forces could cause to the rotor. Therefore, the collective blade pitch is computed as follows:

$$\beta_{CPC} = k_{P,P}\Delta\omega_\epsilon + k_{I,P}\int\Delta\omega_\epsilon dt, \tag{11}$$

where the pitch controller gain constants of the proportional and integral terms are given by $k_{P,P}$ and $k_{I,P}$, respectively. The angular velocity error is given by

$$\Delta\omega_\epsilon = \omega_g - \omega_{rated}, \tag{12}$$

where ω_{rated} is the rated angular velocity of the rotor. If $\beta_{CPC} < 0$ (region 2), then the integral is reset to $-k_{P,P}/k_{I,P}\Delta\omega_\epsilon$, and the baseline CPC controller sets the pitch to $\beta_{CPC} = 0$ and the generator torque is that given by Eq. (10). Else, if $\beta_{CPC} > 0$, then this corresponds to region 2.5–3 and the blades are collectively pitched to the value given by Eq. (11) and the generator torque is given by

$$\tau_g = \frac{\pi \rho R^5 C_{p,\max}}{2\lambda_{opt}^3 G^3}\omega_g^2 + k_{P,T}\Delta\omega_\epsilon + k_{I,T}\int\Delta\omega_\epsilon dt, \tag{13}$$

where the torque controller gain constants are given by $k_{P,T}$ and $k_{I,T}$. If the generator torque command saturates to its rated value (region 3), it remains constant at $\tau_g = \tau_{rated}$ and the angular velocity is managed by the PI CPC. A schematic of the control architecture is shown in Fig. 2.

D. Individual pitch control system (IPC)

The objective of the implemented IPC is to mitigate 1P load fluctuations on the blades due to the heterogeneity of the flow impinging into the rotor. P is the rotational frequency of the blade. However, the dependence of the rotor dynamics on its angular position makes it a periodic dynamical system for which standard linear time-invariant controllers may not be suitable. Therefore, rotating quantities are projected onto a non-rotating coordinate system by performing a multi-blade coordinate (MBC) transformation.[30] The out-of-plane blade root bending moment is projected into the cyclic bending moment as follows:[30]

$$\begin{bmatrix} M_{\cos} \\ M_{\sin} \end{bmatrix} = \begin{bmatrix} \cos(\phi) & \cos\left(\phi + \frac{2}{3}\pi\right) & \cos\left(\phi + \frac{4}{3}\pi\right) \\ \sin(\phi) & \sin\left(\phi + \frac{2}{3}\pi\right) & \sin\left(\phi + \frac{4}{3}\pi\right) \end{bmatrix}\begin{bmatrix} M_1 \\ M_2 \\ M_3 \end{bmatrix}, \tag{14}$$
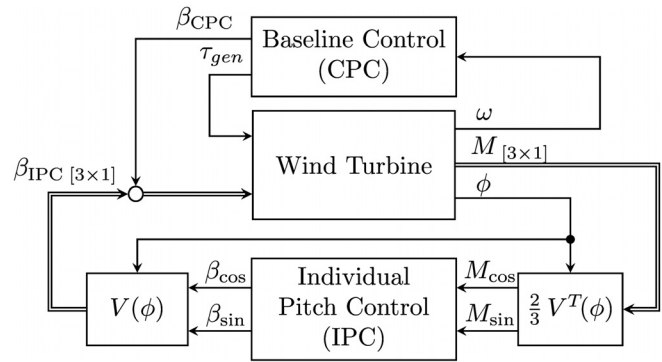

FIG. 2. Control architecture for individual blade-pitch control. The parameter M is the blade root bending moment, ϕ is the angular position of the rotor, V is the multi-blade coordinate transformation tensor, $M_{\cos}$ and $M_{\sin}$ are the projection of the cyclic blade root bending moment, $\beta_{\cos}$ and $\beta_{\sin}$ are the two cyclic blade pitch signals, β_{IPC} and β_{CPC} are the individual and collective pitch commands, respectively, τ_{gen} is the generator torque, and ω is the rotor angular velocity.

where ϕ is the angular position of the rotor and M_1, M_2, and M_3 are the out-of-plane root bending moments of each blade. Two cyclic control signals, $\beta_{\cos}$ and $\beta_{\sin}$, are generated by two SISO integral loop controllers given by the following equations:

$$\beta_{\cos}(t) = k_{\cos}\int_0^t M_{\cos}(\tau)d\tau, \tag{15}$$

$$\beta_{\sin}(t) = k_{\sin}\int_0^t M_{\sin}(\tau)d\tau, \tag{16}$$

where $k_{\cos}$ and $k_{\sin}$ are tunable gains. The resulting signals are projected into the rotating frame to obtain the following:

$$\begin{bmatrix} \beta_{1,IPC} \\ \beta_{2,IPC} \\ \beta_{3,IPC} \end{bmatrix} = \begin{bmatrix} \cos(\phi) & \cos\left(\phi + \frac{2}{3}\pi\right) & \cos\left(\phi + \frac{4}{3}\pi\right) \\ \sin(\phi) & \sin\left(\phi + \frac{2}{3}\pi\right) & \sin\left(\phi + \frac{4}{3}\pi\right) \end{bmatrix}^T \begin{bmatrix} \beta_{\cos} \\ \beta_{\sin} \end{bmatrix}, \tag{17}$$

where $\beta_{1,IPC}$, $\beta_{2,IPC}$, and $\beta_{3,IPC}$ are the pitch command for each blade. The resulting individual pitch command is superimposed on the collective pitch command from the baseline controller.

E. Aeroelastic model

The implemented structural blade model uses a second-order non-linear Euler–Bernoulli beam theory to describe the deflection of the blade, as follows:[17]

$$m\left(\frac{\partial^2 d_1}{\partial t^2} + \frac{\partial^2 \vartheta}{\partial t^2}l_{cg}\cos(\varphi)\right) + F_{d_1,1} + F_{d_1,2} + F_{d_1,3} + F_{d_1,4}$$

$$= f_{d_1} + \frac{\partial\left(\frac{\partial d_1}{\partial s}\int_s^R f_w d\rho\right)}{\partial s}, \tag{18}$$

$$m \left(\frac{\partial^2 d_2}{\partial t^2} - \frac{\partial^2 \vartheta}{\partial t^2} l_{cg} \sin(\varphi) \right) + F_{d_2,1} + F_{d_2,2} + F_{d_2,3} + F_{d_2,4}$$

$$= f_{d_2} + \frac{\partial \left[\left(\frac{\partial d_2}{\partial s} + l_{pi} \right) \int_s^R f_w d\rho \right]}{\partial s}, \tag{19}$$

where d_1 and d_2 are the blade deflection from its undeformed position along the out-of-plane and in-plane direction, respectively, and ϑ is the torsional deformation at blade span s. The distance from the center of rotation of the pitch to the elastic axis is given by l_{pi} and the distance from the elastic axis to the center of gravity is given by l_{cg} (see Fig. 3). External forces such as aerodynamic loads along the flap width and edge direction are given by f_{d_1} and f_{d_2}, respectively, while the forces along the blade span are given by f_w. The force terms $F_{d,1}$, $F_{d,2}$, $F_{d,3}$, and $F_{d,4}$ take into account the rotor speed, gravity, blade stiffness, and the angular acceleration of the rotor, respectively. Although the model includes a description of the axial deformation of the blade, the torsional effects were neglected in this work. However, although the torsion of the blade contributes to the general decrease in the aerodynamic loads, as noted by della Posta et al.,[16] the torsional fluctuations are of small amplitude. Therefore, they may not contribute significantly to the unsteadiness of the blade compared to the effect of gravity and aerodynamic loads along the in-plane and out-of-plane directions. Thus, the torsional effect on the analysis of the blade deformation and load variation and spectra shown below can be neglected. For more details on the structural model, the reader is referred to Kallesøe.[17]

The blade deformation equations [Eqs. (15) and (16)] are discretized in space using a second-order finite difference scheme and advanced in time using the semi-implicit Crank–Nicolson scheme. The resulting system of equations is solved by performing an LU decomposition to the coefficient matrix combined with forward and backward substitution. Subsequently, the blade deformation is applied to the unstructured Lagrangian grid to sample the flow velocity at the blade and the distribution of the aerodynamic loads from and into the Eulerian flow grid, respectively.
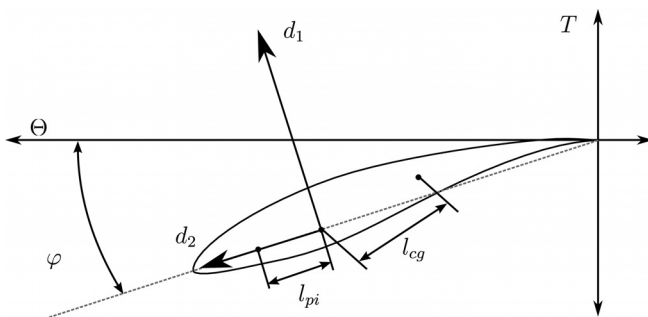
F. Coupling of the VFS-Wind LES flow solver with control systems and aeroelastic model

In the VFS-Wind code, the LES flow solver, the actuator surface model, turbine control, and structural model are compartmentalized in four modules, as shown in Fig. 4. The main module solves the spatially filtered Navier–Stokes equations [Eqs. (1) and (2)] to obtain the flow state, Q_n, at time t_n. This module shares the velocity field, u_n, with the actuator surface module to compute the aerodynamic loads, $f_{l,n}$, over the blade and the aerodynamic torque, $\tau_{a,n}$.

The turbine control module computes the generator torque and the blade pitch angle, β_{n+1}, as discussed in Secs. II C and II D. The new angular position of the rotor, θ_{n+1}, is computed from the balance of angular momentum given by

$$I \frac{d\omega}{dt} = \tau_{a,n} + \tau_{g,n}, \tag{20}$$

where I is the rotational inertia of the turbine rotor, and $\tau_{g,n}$ is the generator torque. An explicit Euler numerical scheme is used to advance the rotor dynamic equation in time. Therefore, the new angular position of the rotor, θ_{n+1}, is given by

$$\theta_{n+1} = \theta_n + \frac{\Delta t}{I}(\tau_{a,n} + \tau_{g,n}). \tag{21}$$

The structural model is coupled with the turbine control and actuator modules. Therefore, the control module shares a subset of state variables, c_n, that is, rotor angular position, velocity and acceleration, and the blade pitch, with the aeroelastic model. In addition, the actuator surface module transfers the aerodynamic loads, $f_{l,n}$, obtained at time t_n to calculate the deflections of the blade, d_n. Moreover, in the two-way coupling method,[15,16] the deflection velocity, $\dot{d}_n$, is computed

FIG. 3. Schematic of a blade cross section that rotates along the rotor plane Θ. The flapwise and edgewise deflection is given by d_1 and d_2, respectively. The l_{cg} and l_{pi} are the distances of the center of gravity and center of gravity to the elastic axis, respectively. The twist of the blade is given by φ.
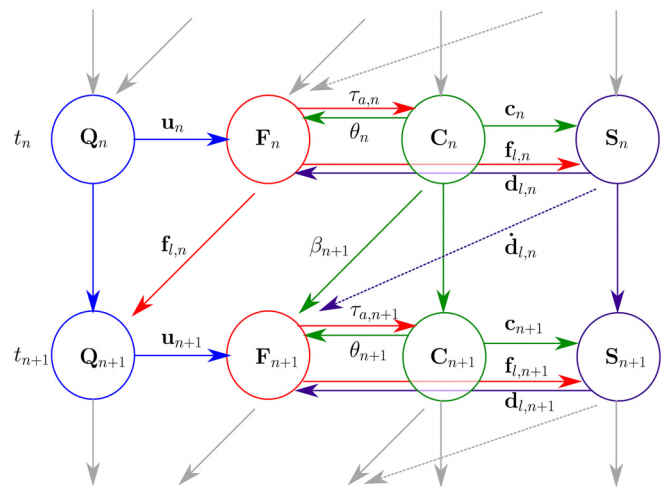
FIG. 4. Schematic of the coupling between the LES flow solver (blue circle), actuator surface/line model (red circle), turbine controller (green circle), and aeroelastic model (purple circle). The parameter Q is the flow state variable, F is the turbine blade aerodynamic state variable, C is the control system state variable, and S is the blade aeroelastic state variable. The shared variables among various modules are the aerodynamic torque, τ_a, the position of the rotor θ, the blade pitch β, and the flow velocity, u, to compute the aerodynamic forces, f, and the blade deflection, d, which are then applied to the equations of fluid motion.

08 April 2024 03:48:04

at time t_n and considered in the calculation of the blade relative velocity, U_{rel}, and the angle of attack, α, as follows:

$$U_{rel} = \sqrt{\left(U_x - \dot{d}_1\right)^2 + \left(U_\theta - \omega r - \dot{d}_2\right)^2}, \quad (22)$$

$$\alpha = \left(\frac{U_x - \dot{d}_1}{U_\theta - \omega r - \dot{d}_2}\right) - \varphi. \quad (23)$$

The newly calculated blade relative velocity and angle of attack [Eqs. (19) and (20)] are used for the computation of the aerodynamic loads at time t_{n+1}. Alternatively, in the one-way coupling method, the relative velocity and angle of attack are given by Eqs. (5) and (6), respectively. The computed blade deflections are shared with the actuator surface module to compute the displacement of the unstructured Lagrangian grid of the blades. The new position of the blade, in turn, is used for the projection of the aerodynamic loads, f_n, into the Eulerian grid used by the flow solver for the computation of the new state at time t_{n+1}, that is, Q_n. The new flow state is also utilized for sampling the velocity field over the blades to calculate the loads for the next time step. Furthermore, it is important to mention that the flow (Q), actuator surface (F), control (C), and structural (S) modules are loosely coupled, which means that each state variable is computed once per time step.

G. Validation of the fluid–structure interaction aeroelastic module in VFS-Wind

The aeroelastic blade model was previously validated by comparing the natural mode of vibrations, steady-state deflections, and aeroelastic stability of the National Renewable Energy Lab (NREL) 5 MW turbine blade[31] against numerical results obtained from the HWACStab and HWC2.[17,32] The HWAC2 and its stability analysis tool, HWACStab, is an aeroelastic code that models the wind turbine structure using a finite beam element method and the blade aerodynamic loads using the blade element method.[33] However, to the best of our knowledge, the model has not been previously implemented into an LES code or coupled with a CFD model of wind turbines.

In this section, we validate the aeroelastic model of Kallesøe[17] as implemented into the VFS-Wind code by applying the code to simulate FSI of the NREL 5 MW wind turbine, for which the blade structural data and thorough analysis of the blade are available.[31] The rotor blades and nacelle are parameterized using the actuator surface model. The computational domain is $10.7D \times 7.9D \times 5.3D$ along the

streamwise, wall-normal, and spanwise directions, respectively, where D is the diameter of the rotor (126 m). A uniform grid resolution is considered along the streamwise direction of $x/D = 0.04$ and the spanwise direction of $z/D = 0.02$. Along the wall-normal direction, a uniform grid resolution of $y/D = 0.02$ is considered up to a height of $1.6D$ and stretched to the top of the domain. As a result, the rotor-swept area is discretized by 50 grid cells along its diameter.

No-slip boundary condition is prescribed at the surface of the terrain with the free-slip boundary condition at the top of the domain, and periodic boundary conditions along the spanwise direction. A uniform velocity is prescribed at the inlet. Simulations are performed for four different wind speeds of $U_\infty = 5.5$, 6.5, 7.5, and 8.5 m/s. The turbine is placed at $5D$ downwind from the inlet, centered along the spanwise direction, and at a hub height of $0.7D$. The structural and aerodynamic descriptions of the blade are obtained from the NREL 5 MW turbine reference manual.[31] The aerodynamic forces obtained from the actuator surface model are interpolated into a one-dimensional Lagrangian grid where the blade deflection equations [Eqs. (18) and (19)] are discretized using 75 grid nodes for each blade.

FSI LES is carried out for an initial transient time interval until the kinetic energy within the flow domain reaches a quasi-steady state. These early transient simulations are discarded and the FSI simulations continue until the first- and second-order turbulent flow statistics have converged. The so-computed blade tip deflection instantaneous data are phase-averaged and compared with the numerical results obtained from the FAST model and provided in the turbine reference manual.[31] To calculate the blade deflection, the OpenFAST model uses the BeamDyn module, which computes aeroelastic of the turbine blades behavior using the geometrically exact beam theory[34] and discretized using Legendre spectral finite elements.[35] An additional simulation of the blade deflection was performed with OpenFAST for a uniform velocity of $U_\infty = 8.5$ m/s to compare the cyclic blade deflection against the results from the aeroelastic model.

A comparison of the phase-averaged blade deflection for $U_\infty = 8.5$ m/s is shown in Fig. 5. The in-plane deformation of the blade [Fig. 5(a)] seems to be caused mainly by its weight, having a sinusoidal deformation as the blades rotate with a maximum and minimum deflection at $\pi/2$ and $3\pi/2$, respectively. Compared with the results obtained from the OpenFAST model, both of our one-way and two-way coupling approaches slightly overestimate the amplitude of the blade deformation. This difference in amplitude is caused by the non-linear geometrical coupling of the in-plane and out-of-plane deformation considered in Kallesøe's model, which is neglected in the
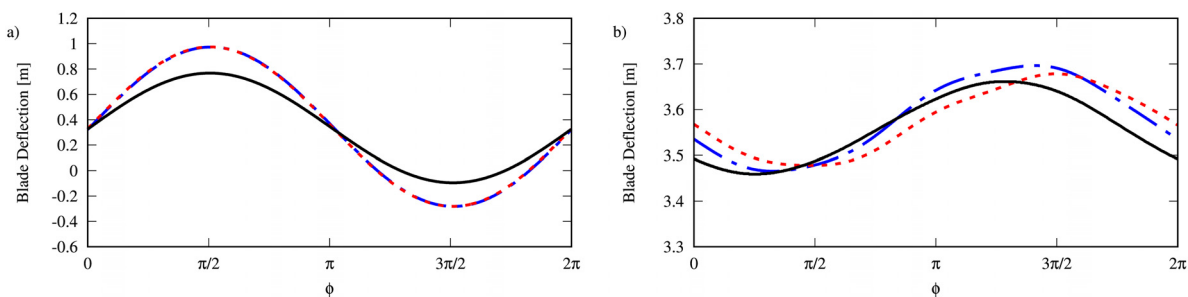

FIG. 5. Phase-averaged in-plane (a) and out-of-plane (b) blade deflection of the NREL 5 MW wind turbine obtained from (solid black lines) OpenFast, (dashed red lines) VFS-Wind with two-way coupled FSI model, and (dashed-dotted blue lines) VFS-Wind with one-way coupled FSI model. ϕ denotes the angular position of the blade.
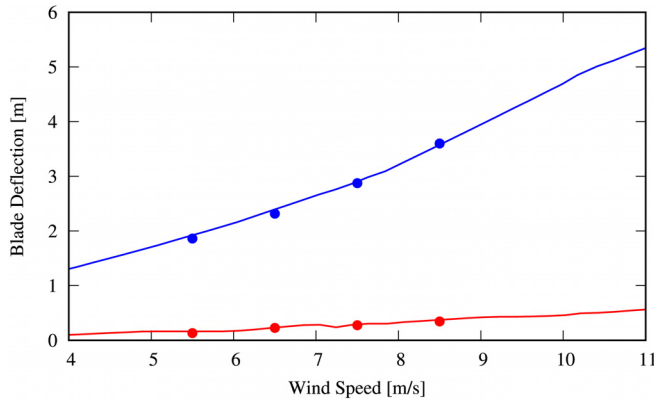
FIG. 6. Time-averaged blade deflection of the NREL 5 MW wind turbine along the (red) in-plane and out-of-plane (blue) direction; (solid lines) reference manual and (filled circles) VFS-Wind one-way coupling.

OpenFast BeamDyn module. Moreover, it seems that the coupling approaches do not affect the in-plane deformation of the blade, as the two curves of the one-way and two-way coupling methods collapse into each other. This is consistent with the findings of della Posta et al.[15,16] for the in-plane deformation of blades using the one- and two-way coupling methods. Slight differences are observed in the out-of-plane deformation of the blades [Fig. 5(b)]. In addition to the difference in the mean and amplitude of the deformation, a phase shift can be seen for the deformation of the blade. These minor differences aside, as seen in Fig. 6, our simulation results for the time-averaged blade deflection agree reasonably well with those obtained from the OpenFAST model.

III. TEST CASE AND COMPUTATIONAL DETAILS

The test case we employ to apply and demonstrate the potential of the VFS-Wind code with aeroelastic and control modules is the Clipper Liberty C96 turbine from the Eolos wind energy research group at the University of Minnesota. The turbine has a rotor diameter of 96 m at a hub height of 80 m and a nameplate capacity of 2.5 MW. Maximum power production of the turbine is obtained at its rated wind speed of 12.5 m/s, with a cut-in velocity of 3 m/s, at which the turbine starts producing power. The turbine operation is stopped at the cutoff velocity of 25 m/s. Control parameters are shown in Table I.

The turbine was placed on a flat terrain with dimensions $14D \times 7D \times 10.4D$ along the streamwise, spanwise, and vertical directions, respectively (Fig. 7). The number of computational grid points is $281 \times 143 \times 281$ along the streamwise, spanwise, and wall-normal directions, respectively, resulting in a resolution of $\Delta x/D = 0.050$ and $\Delta z/D = 0.025$ in streamwise and spanwise directions, respectively.

TABLE I. Turbine control parameters.

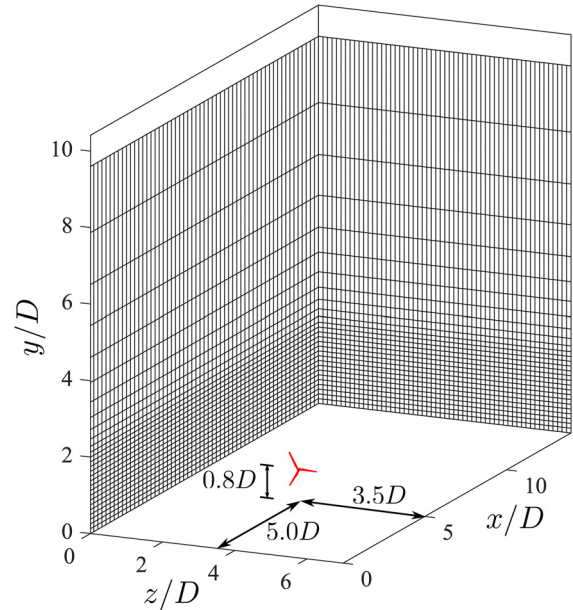| $C_{P,\max}$	0.49	$K_{I,P}$	3.87×10^{-3}
λ_{opt}	8.3	$K_{P,T}$	88.47 N N m s
R	73.13	$K_{I,T}$	11.05
G	48 m	$K_{\cos}$	2.0×10^{-4} N^{-1} m^{-1} s^{-1}
$K_{P,P}$	3.11×10^{-2} s	$K_{\sin}$	2.0×10^{-4} N^{-1} m^{-1} s^{-1}

FIG. 7. Geometrical configuration of the computational domain. The Eulerian grid system (solid lines) is shown for every other five computational cells. The blade and nacelle unstructured grid system are represented in red (red). The rotor diameter is D, and wind flows along the x axis.

In the vertical direction, the grid has a uniform resolution of $\Delta y/D = 0.025$ up to a height of $y/D = 2.1$, above which the grid is gradually stretched to the top of the domain. The turbine was located at $x/D = 5$ downstream from the inlet and centered in the spanwise direction.

The Reynolds number ($Re = U_\infty D/\nu$) of the numerical simulations is 5×10^8. Periodic boundary conditions are imposed along the spanwise direction, while a free-slip boundary condition is applied at the top of the domain. A wall model is used to specify boundary conditions on the ground assuming a logarithmic law of the wall, as follows:

$$U = \frac{U_*}{\kappa} \ln \frac{z}{z_0},\qquad(24)$$

where U_* is the friction velocity, κ is the von Karman constant, and z_0 is the roughness length ($z_0 = 0.1$ m). A precursor simulation with periodic boundary condition was performed to generate a fully developed neutral atmospheric boundary layer. The initial transient of the precursor simulation was discarded, and simulations continued until the total kinetic energy in the flow domain reached a quasi-steady state. Subsequently, instantaneous velocity fields from the precursor simulation were recorded and fed at the inlet of the wind turbine simulation (for more details, see Refs. 36 and 37). The wind shear exponent of the precursor simulation is $\alpha = 0.2$. This considered value is larger than that of the FAST simulations reported in Ossmann et al.,[7,38] in which the wind shear exponent was set to 0.14.

IV. RESULTS AND DISCUSSION

A series of FSI-LES with control systems were carried out for the Eolos wind turbine to examine the performance of CPC and IPC

control modules and their impact on the blade deflection. Five different hub-height wind speeds of $U_{hub} = 7.0$, 8.5, 10.0, 11.7, and 14.0 m/s were considered, when the turbine operates in regions 2.0, 2.5, and 3. The deflections of the blades were modeled using the one-way and two-way aeroelastic model. A series of benchmark simulations with the baseline CPC were carried out for each case to provide benchmarks for the simulation results with IPC. An additional set of simulations with rigid blades, that is, without aeroelastic model, was conducted to assess the effect of rigid blade assumption on the turbine wake flow field and the computed loads.

A. Blade deflection

The time variation of the blade tip in-plane and out-of-plane deflections obtained from the two-way coupled model is shown in Fig. 8. Results are shown for the cases with the hub-height speed of $U_{hub} = 7.0$ and 14.0 m/s. The out-of-plane deflection of the blade [Figs. 8(a) and 8(b)] shows low-frequency fluctuations that seem to be due to the impingement of the large coherent turbulent structures into the turbine rotor. As seen, the case with the higher hub-height velocity presents larger variations. However, due to the pitching action of the IPC, the high-frequency fluctuations are clearly dampened by the controller, suggesting that these fluctuations are due to the uneven loads across the turbine rotor. Similarly, the in-plane deflection of the blade [Figs. 8(c) and 8(d)] shows low-frequency fluctuations caused by variations of the velocity. The high-frequency fluctuations seem to correspond to the rotation of the turbine. The IPC has a negligible effect on the blade in-plane deformation fluctuations as the simulation results of the two controllers seem to roughly overlap.

The phase-averaged tip deflections are calculated to quantify the deflection through the blade revolution (Fig. 9). As seen in Figs. 9(a) and 9(b), the out-of-plane blade deflection is higher near $\phi = 0$ and 2π, which correspond to the turbine blade when it is at its highest elevation during the revolution. Also, as seen, the minimum deflection occurs when the blade is at the lowest elevation ($\phi = \pi$). However, it is observed that the maximum and minimum deflections do not perfectly coincide with the maximum and minimum bending moments. This is caused by the natural response observed as fluctuations superimposed to the sinusoidal deflection due to the uneven loading of the rotor. Moreover, the IPC shows to have a negligible effect in the in-plane deflection of the blade [Figs. 9(c) and 9(d)]. This indicates that the in-plane deformation of the blade is mainly driven by the blade weight, as it was also observed from the previously presented time series data [Figs. 8(c) and 8(d)].

To examine the effect of controllers on the blade deflection at different frequencies, the power spectral density of the simulation results for the blade tip deflection was calculated. Spectra of the blade tip deflection moment were computed as

$$E_{d_i}(f) = \int R_{d_i}(s)e^{-i2\pi fs}ds, \tag{25}$$

where the autocovariance, R_{d_i}, of the blade deflection fluctuations, d'_i, is given by

$$R_{d_i}(s) = \overline{d'_i(t)d'_i(t+s)}. \tag{26}$$

Figure 10(a) shows the spectra of the out-of-plane deflection with the IPC and CPC at various hub-height wind speeds. As seen, the spectra at different wind speeds present peaks of energy at the
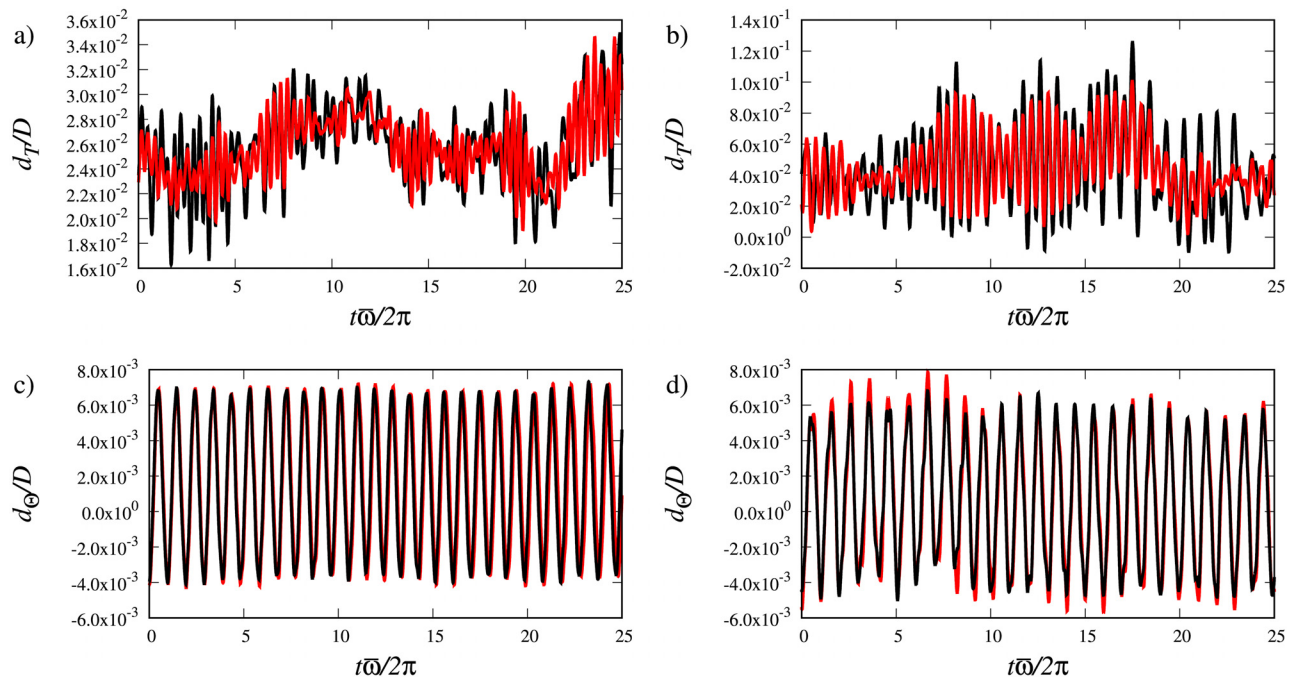

FIG. 8. Time variation of the blade tip deflection along the (a) and (b) out-of-plane and (c) and (d) in-plane direction for $U_{hub} = 7.0$ m/s (a) and (c) and 14.0 m/s (b) and (d) for the turbine with the CPC (solid black lines) and the IPC (solid red lines). Obtained from VFS-Wind two-way coupled structural model. D is the rotor diameter, and $\overline{\omega}$ is the rotor time-averaged angular velocity.
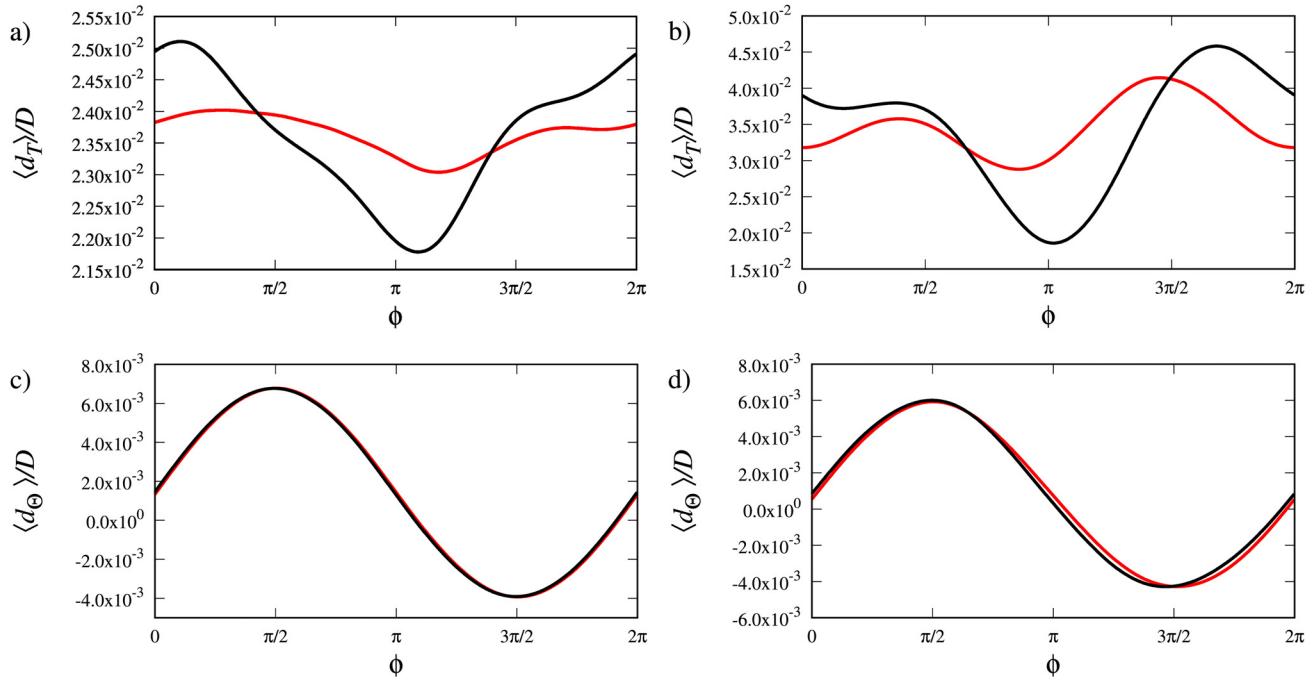
FIG. 9. Phase-averaged blade tip deflection along the (a) and (b) out-of-plane and (c) and (d) in-plane direction for U_{hub} = 7.0 m/s (a) and (c) and 14.0 m/s (b) and (d) for the turbine with CPC (solid black lines) and the IPC (solid red lines). Obtained from VFS-Wind two-way coupled structural model. *D* is the rotor diameter.

rotational frequency of the turbine rotor ($f 2\pi/\overline{\omega} = 1$) and their harmonics at $f 2\pi/\overline{\omega} = 2$. Another energy peak is observed between $f 2\pi/\overline{\omega} = 3$ and $f 2\pi/\overline{\omega} = 2$, for the various hub-height wind speed cases. The energy of this peak seems to exceed those of their harmonics, owing to the heterogeneity of the velocity at the rotor.

This finding suggests that this energy peak corresponds to the natural frequency response of the blade. To further investigate this, we seek to calculate the natural frequency of the blade and replot Fig. 10 by normalizing the frequencies with the first-mode natural frequency. Assuming that the blade is a homogeneous
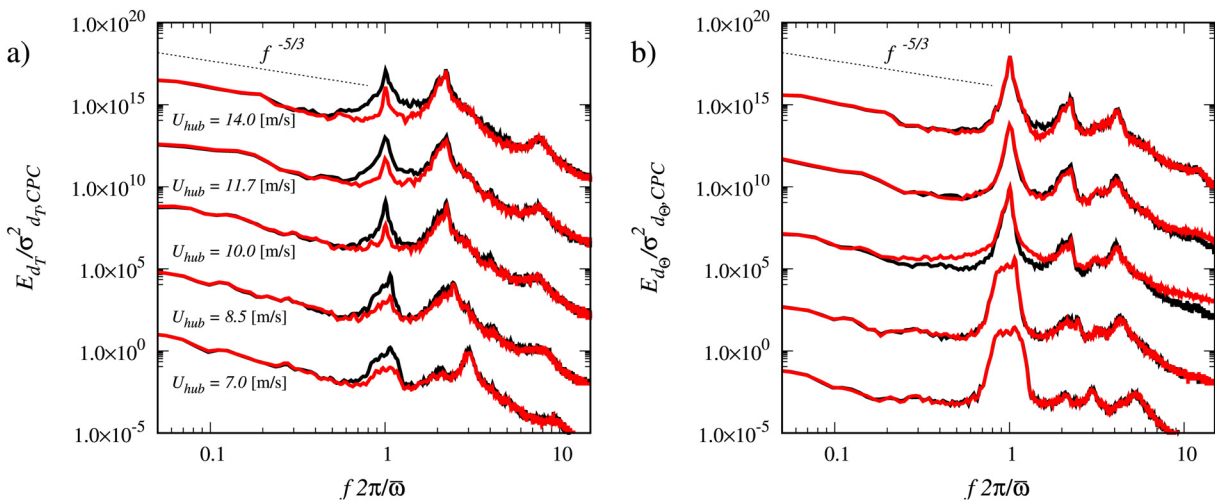

FIG. 10. Spectra of the blade tip deflection normalized by the standard deviation of the deflection of the CPC case along the (a) out-of-plane and (b) in-plane direction for the CPC (solid black lines) and IPC (solid red lines) obtained from VFS-Wind two-way aeroelastic model. The frequency (*f*) is normalized by the time-averaged angular velocity of the rotor ($\overline{\omega}$). Spectra are shifted upward four decades for each hub-height velocity. *E* is the spectra of the blade root bending moment, and σ_{CPC} is the standard deviation of blade deflection of the turbine with CPC.

cantilever beam, the first mode natural frequency can be estimated as

$$f_n = \frac{(1.875)^2}{2\pi} \sqrt{\frac{EI}{\rho_L L^4}}, \quad (27)$$

where E is the blade Young's modulus, I is the blade area moment of inertia, ρ_L is the mass per unit length of the blade, and L is the length of the blade from the root to the tip. By computing the span-averaged blade properties and substituting these values into Eq. (27), the first mode natural frequency of the blade can be estimated as $f_n = 0.6$ Hz. Figures 11(a) and 11(b) show the spectra of the out-of-plane and in-plane deflections, respectively, as a function of the frequency normalized by the so computed first mode natural frequency, that is, $f_n = 0.6$ Hz. As seen in this figure, the peak of energy mentioned above is observed at $f/f_n = 1$, confirming that it corresponds to the first-mode natural frequency of vibration of the blade.

As it was shown in this section, the IPC seems to effectively reduce the energy of the out-of-plane blade deflection fluctuations caused by the uneven loading at the rotor observed at $f\,2\pi/\overline{\omega} = 1$ [Fig. 10(a)]. However, the IPC did not impact the energy at the natural vibration of the blade, marked by similar energy at $f/f_n = 1$ [Figs. 11(a) and 11(b)]. Moreover, the spectra of the in-plane deflection [Fig. 10(b)] show that the IPC had a negligible effect on the energy of the in-plane blade deflection fluctuations.

B. Wind turbine loads and mean flow characteristics

A comparison of the time variation of the blade root bending moment for the turbine with CPC and IPC with the two-way aeroelastic model and the rigid blades is shown in Fig. 12. Because of the similarity of the simulations results for different hub-height velocities, and for the sake of brevity, only the results for $U_{hub} = 7.0$ and 14 m/s are discussed. Also, it should be clarified that due to the coupling between the aeroelastic and actuator surface models, the bending moments

presented in this work are obtained from the aerodynamic loads over the turbine blades. Similar to what is observed for the time variations of the blade tip deflection, the time variations of the bending moment with the baseline CPC [Figs. 12(a) and 12(c)] mark low-frequency fluctuations that are caused by the large coherent turbulent structures impinging upon the turbine rotor. Moreover, high-frequency fluctuations are also observed induced by the heterogeneity of the velocity across the turbine rotor. However, as seen in Figs. 12(b) and 12(d), the IPC decreases the magnitude of these higher frequency fluctuations. Only minor differences are observed for the magnitude of the fluctuations obtained from the aeroelastic model and the rigid blade for the CPC and IPC. These minor variations result from the differences in the probe location of velocity sampling for the load calculations from the Eulerian grid to the Lagrangian grid of the blade, which is deflected for the aeroelastic model.

The spectra of the blade root bending moment normalized by the standard deviation of the CPC signal are shown in Fig. 13. A peak in the spectra is observed for the CPC cases at $f\,2\pi/\overline{\omega} = 1$ (and its harmonics) caused by the uneven loading of the blades due to the heterogeneity of the velocity across the rotor—as observed for the blade deflection spectra. As shown in the time variation of the bending moment [Figs. 12(b) and 12(d)], the pitch action of the turbine blade with the IPC suppresses the spectral energy at this frequency ($f\,2\pi/\overline{\omega} = 1$). Figure 13(b) shows a zoomed-in view of the spectra in the region of the peak for the case with $U_{hub} = 7.0$ m/s. As seen, the FSI simulations reveal a higher energy of fluctuations than the rigid blade simulations at the frequency $f\,2\pi/\overline{\omega} = 1$. The same trend was also observed for all simulated hub-height velocities. This trend reveals that by modeling the blade as rigid, it may underestimate the fatigue loads on the blade due to the heterogeneity of the wind speed impinging into the rotor.

Finally, and as illustrated in Fig. 14, the effect of the blade deflection on the computed time-averaged streamwise velocity in the wake of the turbine is indiscernible for all cases. As seen, the velocity profiles obtained for the aeroelastic, and rigid blade cases overlap.
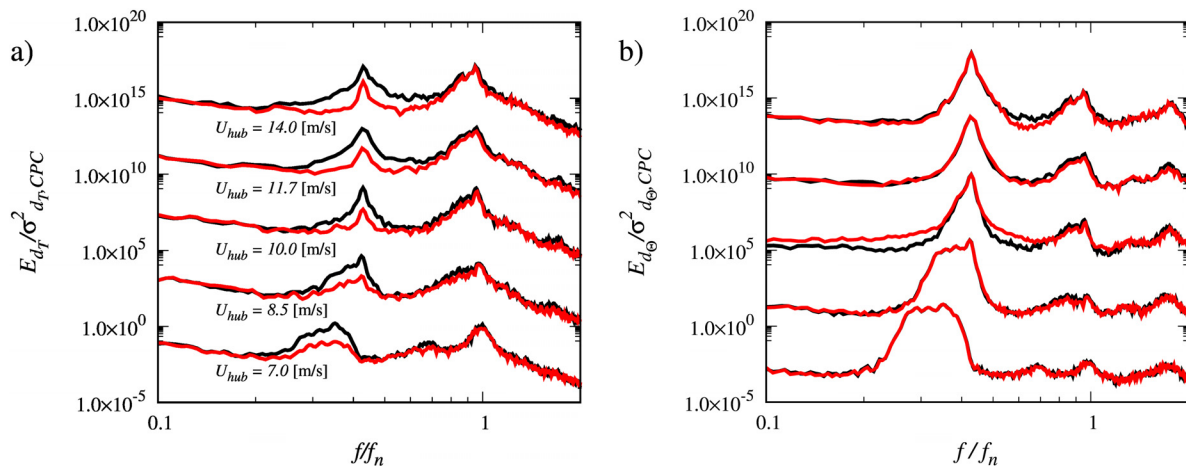

FIG. 11. Spectra of the blade tip deflection normalized by the standard deviation of the deflection of the CPC case along the (a) out-of-plane and (b) in-plane direction for the CPC (solid black lines) and IPC (solid red lines) obtained from VFS-Wind two-way aeroelastic model. The frequency (f) is normalized by the first-mode natural frequency (f_n), obtained from Eq. (27). Spectra are shifted upward four decades for each hub-height velocity. E is the spectra of the blade root bending moment and σ_{CPC} is the standard deviation of blade deflection of the turbine with CPC.
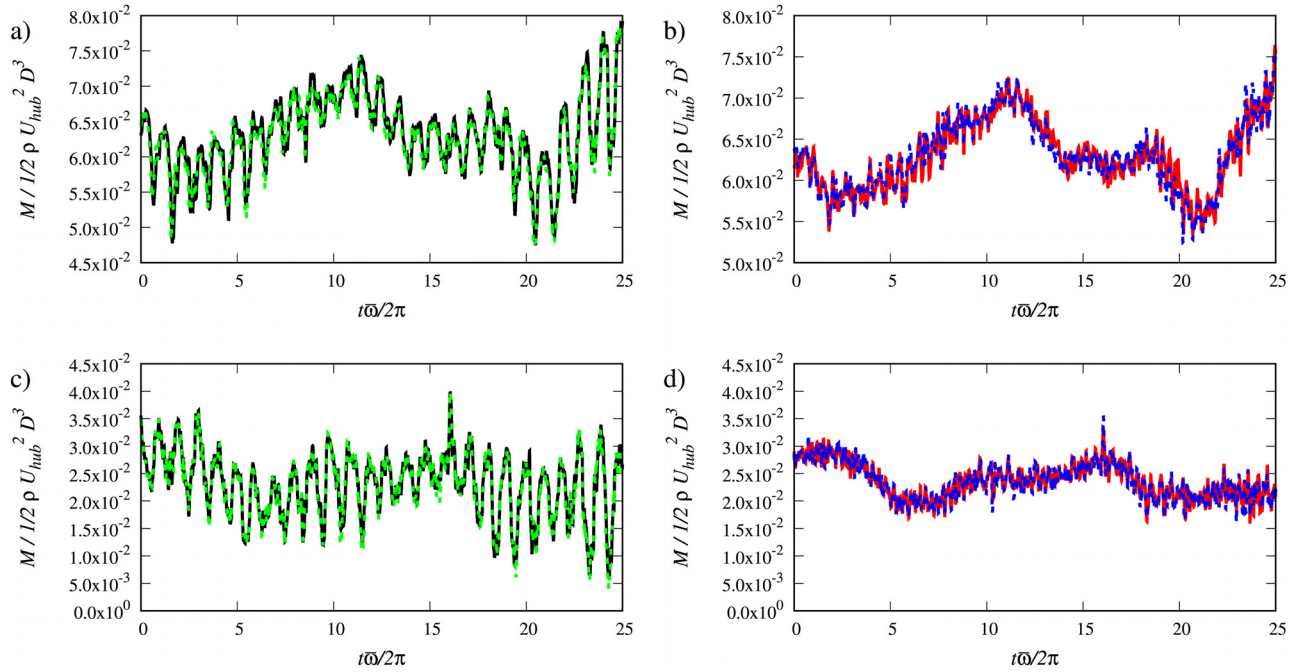
FIG. 12. Time variation of the bending moment at the root of a single turbine blade. (a) and (c) CPC results with (solid black lines) aeroelastic model and (dashed green lines) rigid blade. (b) and (d) IPC results with (solid red lines) two-way coupled aeroelastic model and (dashed green lines) rigid blade. Hub-height velocities are 7.0 m/s (a) and (b) and 14.0 m/s (c) and (d), respectively. M is the root bending moment, ρ is the fluid density, U_{hub} is the hub-height velocity, D is the rotor diameter, and $\overline{\omega}$ is the rotor time-averaged angular velocity.

This indicates that the mean deflection of the blade does not have a significant effect on the loads over the blade, as it was also observed in the time variation of the bending moment.

C. Effect of the structural model coupling scheme

A three-way comparison of the spectra of the root bending moment fluctuations of the Eolos turbine with rigid blades, and the

one-way and two-way coupled aeroelastic model is shown in Fig. 15. For the sake of comparison, for all three cases we only consider the baseline controller (CPC). The energy spectra of the one-way coupled aeroelastic model seem to be slightly under-estimated compared to the two-way coupled model. Moreover, the zoomed-in view of the energy peak at $f2\pi/\overline{\omega} = 1$ for $U_{hub} = 7$ and 14 m/s in Figs. 15(b) and 15(c) demonstrates that the magnitude of energy of the one-way coupled model is similar to that of the rigid blade. This could be due to the
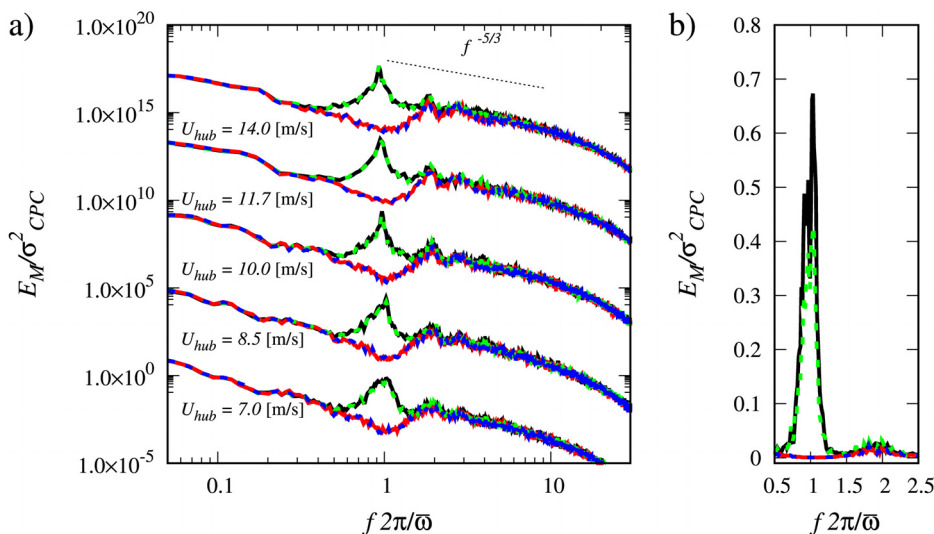

FIG. 13. (a) Spectra of the root bending moment normalized by the standard deviation of the CPC bending moment, σ_{CPC}, of the CPC-FSI (solid black lines), CPC-rigid (dashed green lines), IPC-FSI (solid red lines), and IPC-rigid (dashed blue lines). Spectra are shifted upward four decades for each hub-height velocity. Zoomed-in view of the spectra in the region of the peak for the case with (b) $U_{hub} = 7.0$ m/s. E_M is the spectra of the blade root bending moment, f is the frequency, and $\overline{\omega}$ is the time-averaged angular velocity of the rotor.
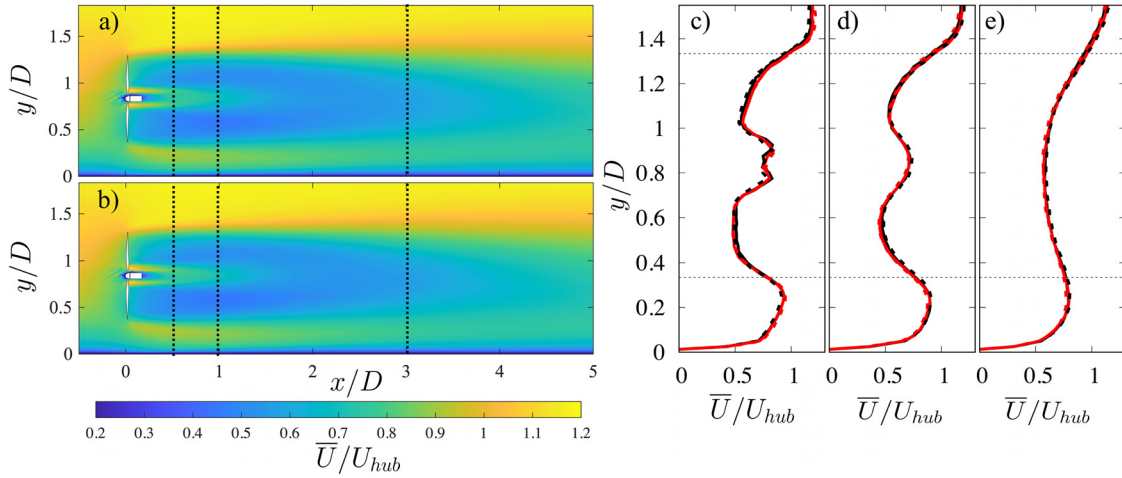
FIG. 14. Contours of the time-averaged streamwise velocity in a vertical section for a hub-height velocity of $U_{hub} = 7.0$ m/s for the aeroelastic (a) and rigid blade (b) case. Vertical profiles of the time-averaged velocity are shown at $0.5D$ (c), $1D$ (d), and $3D$ (e) downstream of the turbine obtained from the aeroelastic case with the CPC (solid black lines) and IPC (solid red lines); and rigid blade case with CPC (dashed black lines) and IPC (dashed red lines).

under resolved blade deflections; that is, the blade deflections are smaller than the grid resolution. We note that under-resolved deflections would not significantly influence the relative velocity (U_{rel}) and the angle of attack (α) at the blade and, thus, the aeroelastic blade behavior would be perceived to behave like to the rigid blade. However, since the two-way coupling considers the blade deformation velocity in the computation of the aerodynamic loads, the computed root bending moment spectra is more significant.

A comparison of the blade tip deflection spectra for the one-way and two-way coupled aeroelastic model is shown in Fig. 16. The main differences are observed in the energy spectra of the out-of-plane deformation fluctuations [Fig. 16(a)] at the peaks of energy corresponding to the rotational frequency ($f\,2\pi/\overline{\omega} = 1$) and the first-mode natural frequency of the blade ($f_n = 0.6$ Hz). As seen, the one-way coupled aeroelastic model seems to underestimate the deformation of the blade at the rotational frequency of the turbine rotor. As discussed above and shown in Fig. 15, the underestimation of blade deflection by the one-way coupled model is a result of the underestimation of energy of the root bending moment fluctuations. However, it is observed that the energy at the natural frequency of out-of-plane fluctuation of the one-way coupled model is higher than that at the rotational frequency. This suggests that the first natural mode of
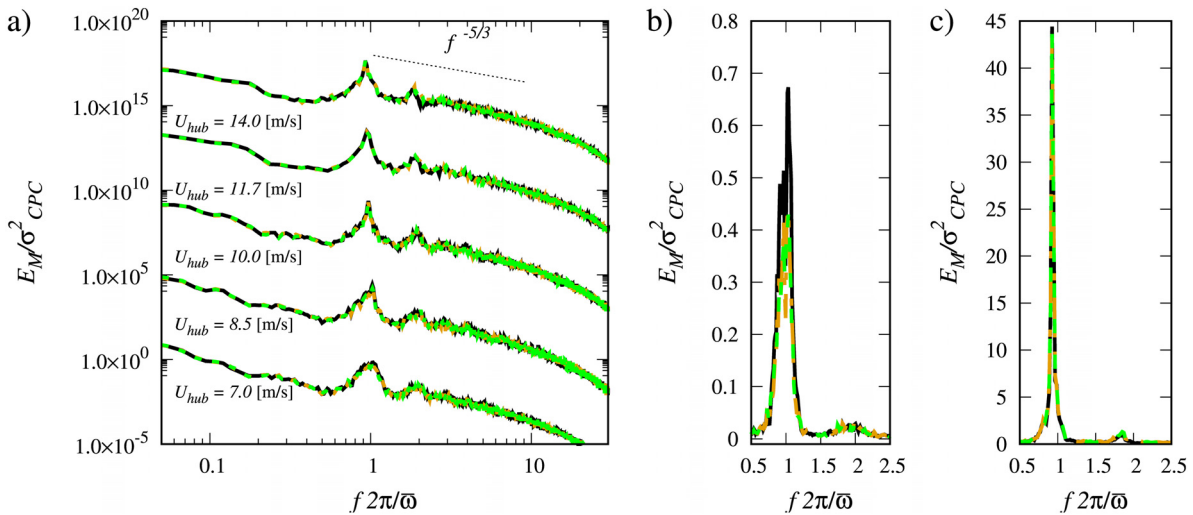

FIG. 15. Spectra of the root bending moment normalized by the standard deviation of the baseline CPC bending moment, σ_{CPC}, obtained from the two-way coupled aeroelastic model (solid black lines), one-way coupled aeroelastic model (dashed yellow lines), and rigid blade (dashed green lines) simulation case. (a) All simulation cases consider the baseline CPC controller. Spectra are shifted upward four decades for each hub-height velocity. Zoomed in of the root bending moment spectra for a hub-height velocity of (b) $U_{hub} = 7.0$ m/s and (c) $U_{hub} = 14.0$ m/s. E_M is the spectra of the blade root bending moment, f is the frequency, and $\overline{\omega}$ is the time-averaged angular velocity of the rotor.
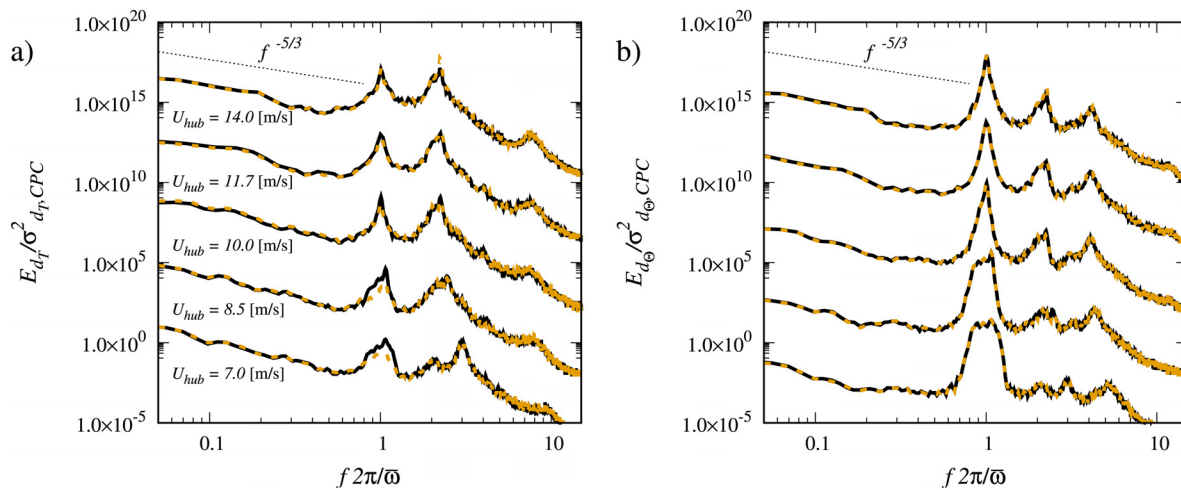
FIG. 16. Spectra of the blade tip deflection normalized by the standard deviation of the deflection of the CPC case along the (a) out-of-plane and (b) in-plane direction of the two-way CPC-FSI (solid black lines) and one-way CPC-FSI (dashed yellow lines) simulation case. The frequency (f) is normalized by the time-averaged angular velocity of the rotor ($\overline{\omega}$). Spectra are shifted upward four decades for each hub-height velocity. E is the spectra of the blade root bending moment, and σ_{CPC} is the standard deviation of blade deflection of the turbine with CPC.

vibrations of the blade dominates the effect of shear flow on the rotor and, thus, its corresponding fluctuations. On the other hand, the spectra of the in-plane fluctuations obtained from the one-way and two-way coupled blade model collapse into each other for every wind speed [Fig. 16(b)]. This indicates that the effect of the aerodynamic loads on the blade in-plane fluctuations is negligible relative to the deformation fluctuations caused by the weight of the blades.

V. CONCLUSIONS

An aeroelastic model was implemented and integrated into our in-house open-source code, the Virtual Flow Simulator (VFS-Wind) model, to describe deformation of the turbine blades enabling realistic investigation of the impact of advanced control systems on the structural performance of wind turbines. The aeroelastic model, originally developed for the aeroelastic behavior of helicopter rotor blades,[17,32] takes into account rotor speed variations and the effect of gravity. The resulting nonlinear partial integral-differential equations were coupled with the blade actuator surface model to compute the blade deflections. The equations of the blade deformation are solved once per time step along with the actuator surface model, resulting in a one-way loose coupling between the models. In addition, a two-way coupling approach,[15,16] which includes the blade deformation velocity in the computation of the aerodynamic loads, was also implemented, and its results were compared against those of the one-way coupled approach. LES of the NREL 5 MW wind turbine was performed to validate the steady-state deformation of the blade. The numerical results obtained from the VFS-Wind model showed a slight overestimation of the in-plane deformation of the blade and a slight phase shift in the out-of-plane blade fluctuations. Nevertheless, the results from the VFS-Wind model agreed well with those obtained with the FAST model.[31]

The coupled LES-aeroelastic-control model was used to study the aeroelastic behavior of the EOLOS Clipper Liberty C96 turbine with the individual pitch control for hub-height wind speeds of $U_{hub} = 7.0$,

8.5, 10.0, 11.7, and 14.0 m/s.[7] Benchmark simulations of the turbine with the baseline CPC were performed to assess the impact of the IPC. Additionally, simulations with rigid blades (i.e., without aeroelastic model) were performed to compare the impact of the aeroelastic modeling on the blade loads and mean flow in the wake of the turbine.

The aeroelastic model did not show a significant impact in the wake of the wind turbine showing similar velocity profiles in the near and far wake of the wind turbine with both the baseline CPC and the IPC. Moreover, the IPC decreased the bending moment fluctuations due to the unbalanced loads over the rotor. The rigid blades were shown to underestimate the load fluctuations, marking marginally less spectral energy at $f\,2\,\pi/\overline{\omega} = 1$ (rotational frequency of the rotor). Analysis of the blade deflection results revealed that the IPC decreases the out-of-plane deflection fluctuations of the blade. Phase-averaged blade deflection showed that the largest out-of-plane deflection occurs when the blade is at the highest position, while the lowest out-of-plane deflection corresponds to the situation where the blade is close to the ground. On the other hand, the IPC had a negligible effect on the in-plane deformation fluctuations of the blade. Nevertheless, fluctuations along the in-plane direction are orders of magnitude smaller than those in the out-of-plane direction, owing to the isotropic structural properties of the blades. In addition, this study shows that the effectiveness of the IPC is to reduce fatigue loads and variation of the blade deflection, which may result in the design of lighter and more flexible blades.

Comparison between the one-way and two-way coupling approaches for the aeroelastic model revealed that, in par with the rigid blade model, the one-way coupling underestimates the root bending moment fluctuations. The underestimation of the blade loads by the one-way coupling approach also resulted in the underestimation of the blade out-of-plane deformation fluctuations obtaining lower spectral energy than the two-way coupling method at the rotational frequency. Nonetheless, the spectral energy of the in-plane deformation fluctuations obtained from the one-way coupling method

was shown to be similar to that of the two-way coupling approach. Given that the two-way coupling approach mainly modifies the computation of the aerodynamic loads, these findings suggest that the in-plane blade fluctuations are primarily driven by the weight of blades.

ACKNOWLEDGMENTS

AUTHOR DECLARATIONS
Conflict of Interest

The authors have no conflicts to disclose.

Author Contributions

Christian Santoni: Conceptualization (equal); Data curation (equal); Formal analysis (equal); Investigation (equal); Methodology (equal); Validation (equal); Visualization (equal); Writing – original draft (equal); Writing – review & editing (equal). **Ali Khosronejad:** Data curation (equal); Formal analysis (equal); Funding acquisition (equal); Investigation (equal); Methodology (equal); Project administration (equal); Resources (equal); Software (equal); Supervision (equal); Validation (equal); Writing – original draft (equal); Writing – review & editing (equal). **Xiaolei Yang:** Conceptualization (equal); Methodology (equal); Software (equal); Writing – review & editing (equal). **Peter Seiler:** Conceptualization (equal); Investigation (equal); Methodology (equal); Software (equal); Writing – review & editing (equal). **Fotis Sotiropoulos:** Conceptualization (equal); Formal analysis (equal); Funding acquisition (equal); Investigation (equal); Methodology (equal); Resources (equal); Software (equal); Supervision (equal); Writing – review & editing (equal).

DATA AVAILABILITY

The data that support the findings of this study are available from the corresponding author upon reasonable request.

REFERENCES

[1]U.S.-Department of Energy, *Wind Vision: A New Era for Wind Power in the United States* (US-Department of Energy, 2015).

[2]A. S. E. Mendoza, S. Yao, M. Chetan, and D. T. Griffith, "Design and analysis of a segmented blade for a 50 MW wind turbine rotor," Wind Eng. **46**, 1146–1172 (2022).

[3]E. Bossanyi, "Developments in closed loop controller design for wind turbines," in *2000 ASME Wind Energy Symposium* (American Institute of Aeronautics and Astronautics, Reston, VA, 2000).

[4]E. A. Bossanyi, "Individual blade pitch control for load reduction," Wind Energy **6**, 119–128 (2003).

[5]M. Geyler and P. Caselitz, "Robust multivariable pitch control design for load reduction on large wind turbines," J. Sol. Energy Eng., Trans. ASME **130**, 031014 (2008).

[6]M. Vali, J. W. van Wingerden, and M. Kuhn, "Optimal multivariable individual pitch control for load reduction of large wind turbines," in *Proceedings of the American Control Conference* (ACC, 2016), pp. 3163–3169.

[7]D. Ossmann, J. Theis, and P. Seiler, "Load reduction on a clipper liberty wind turbine with linear parameter-varying individual blade pitch control," Wind Energy **20**, 1771–1786 (2017).

[8]J. M. Jonkman and M. L. Buhl, Jr., "FAST user's guide," Report No. NREL/EL-500-29798 (Renewable Energy Laboratory, Golden, Colorado, 2005).

[9]T. Larsen and A. Hansen, "Aeroelastic effects of large blade deflections for wind turbines," in Proceedings of the Science of Making Torque from Wind (2004).

[10]T. Larsen, H. Madsen, A. Hansen, and T. Risoe, "Investigation of stability effects of an offshore wind turbine using the new aeroelastic code HAWC2," in Proceedings of Copenhagen Offshore Wind (2005).

[11]C. Santoni, A. Khosronejad, P. Seiler, and F. Sotiropoulos, "Toward control co-design of utility-scale wind turbines: Collective vs. individual blade pitch control," Energy Rep. **9**, 793–806 (2023).

[12]M. J. Churchfield, S. Lee, J. Michalakes, and P. J. Moriarty, "A numerical study of the effects of atmospheric and wake turbulence on wind turbine dynamics," J. Turbul. **13**, N14 (2012).

[13]H. Meng, F.-S. Lien, and L. Li, "Elastic actuator line modelling for wake-induced fatigue analysis of horizontal axis wind turbine blade," Renewable Energy **116**, 423–437 (2018).

[14]Z. Yu, Z. Hu, X. Zheng, Q. Ma, and H. Hao, "Aeroelastic performance analysis of wind turbine in the wake with a new elastic actuator line model," Water **12**, 1233 (2020).

[15]G. della Posta, U. Ciri, S. Leonardi, and M. Bernardini, "A novel two-way coupling method for the study of the aeroelasticity of wind turbines in a large eddy simulation framework," in 14th European Conference on Turbomachinery Fluid Dynamics and Thermodynamics (2021).

[16]G. Della Posta, S. Leonardi, and M. Bernardini, "A two-way coupling method for the study of aeroelastic effects in large wind turbines," Renewable Energy **190**, 971–992 (2022).

[17]B. S. Kallesøe, "Equations of motion for a rotor blade, including gravity, pitch action and rotor speed variations," Wind Energy **10**, 209–230 (2007).

[18]A. Calderer, X. Yang, D. Angelidis, A. Khosronejad, T. Le, S. Kang *et al.*, "Virtual flow simulator," No. VFS-Wind; 004806MLTPL00 (University of Minnesota, 2015).

[19]D. H. Hodges and E. H. Dowell, *Nonlinear Equations of Motion for the Elastic Bending and Torsion of Twisted Nonuniform Rotor Blades* (National Aeronautics and Space Administration, Washington, DC, 1974).

[20]J. C. Heinz, "Partitioned fluid-structure interaction for full rotor computations using CFD," Ph.D. thesis (Technical University of Denmark, 2013).

[21]M. Germano, U. Piomelli, P. Moin, and W. H. Cabot, "A dynamic subgrid-scale eddy viscosity model," Phys. Fluids A **3**, 1760 (1991).

[22]J. Kim and P. Moin, "Application of a fractional-step method to incompressible Navier–Stokes equations," J. Comput. Phys. **59**, 308–323 (1985).

[23]X. Yang and F. Sotiropoulos, "A new class of actuator surface models for wind turbines," Wind Energy **21**, 285–302 (2018).

[24]W. Froude, "On the elementary relation between pitch, slip and propulsive efficiency," Report No. NACA-TM-1 (Inst. Naval Architects, 1878).

[25]Z. Du and M. Selig, "A 3-D stall-delay model for horizontal axis wind turbine performance prediction," in *1998 ASME Wind Energy Symposium* (American Institute of Aeronautics and Astronautics, Reston, VA, 1998).

[26]W. Z. Shen, J. N. Sørensen, and R. Mikkelsen, "Tip loss correction for actuator/Navier–Stokes computations," J. Sol. Energy Eng. **127**, 209 (2005).

[27]F. Schultz-Grunow, "Neues Reibungswiderstandsgesetz für glatte Platten," Luftfahrtforschung **17**, 239–246 (1940).

[28]X. Yang, X. Zhang, Z. Li, and G. W. He, "A smoothing technique for discrete delta functions with application to immersed boundary method in moving boundary simulations," J. Comput. Phys. **228**, 7821–7836 (2009).

[29]T. Burton, D. Sharpe, N. Jenkins, and E. Bossanyi, *Wind Energy Handbook* (Wiley, 2011).

[30]G. Bir, A. Wright, C. Butterfield, G. Bir, A. Wright, and C. Butterfield, "Stability analysis of a variable-speed wind turbine," in 35th Aerospace Sciences Meeting and Exhibit (1997).

[31]J. Jonkman, S. Butterfield, W. Musial, and G. Scott, "Definition a 5-MW reference wind turbine offshore system development," No. NREL/TP-500-38060 (NREL, 2009).

[32]B. S. Kallesøe, "Effect of steady deflections on the aeroelastic stability of a turbine blade," Wind Energy **14**, 209–224 (2011).

[33]M. H. Hansen, "Aeroelastic stability analysis of wind turbines using an eigenvalue approach," Wind Energy **7**, 133–143 (2004).

[34]D. H. Hodges, *Nonlinear Composite Beam Theory* (American Institute of Aeronautics and Astronautics, Reston, VA, 2006).

[35]Q. Wang, M. A. Sprague, J. Jonkman, N. Johnson, and B. Jonkman, "BeamDyn: A high-fidelity wind turbine blade solver in the FAST modular framework," Wind Energy **20**, 1439–1462 (2017).

[36]W. R. Oaks, K. Flora, and A. Khosronejad, "Eulerian numerical modeling of contaminant transport in lower Manhattan, New York City, from a point-source release under the dominant wind condition: Insights gained via LES," Atmos. Environ. **262**, 118621 (2021).

[37]A. Khosronejad, K. Flora, and S. Kang, "Effect of inlet turbulent boundary conditions on scour predictions of coupled LES and morphodynamics in a field-scale river: Bankfull flow conditions," J. Hydraul. Eng. **146**, 04020020 (2020).

[38]D. Ossmann and J. Theis, "Multivariable controller design verification for a Liberty wind turbine," in *35th Wind Energy Symposium* (AIAA, 2017).

08 April 2024 03:48:04